Monthly Notices of the ROYAL ASTRONOMICAL SOCIETY
MNRAS **443,** 1810–1820 (2014) doi:10.1093/mnras/stu1199

Warm ice giant GJ 3470b – II. Revised planetary and stellar parameters from optical to near-infrared transit photometry

Lauren I. Biddle,[1⋆] Kyle A. Pearson,[1] Ian J. M. Crossfield,[2] Benjamin J. Fulton,[3] Simona Ciceri,[2] Jason Eastman,[4] Travis Barman,[5] Andrew W. Mann,[3] Gregory W. Henry,[6] Andrew W. Howard,[3] Michael H. Williamson,[6] Evan Sinukoff,[3] Diana Dragomir,[4] Laura Vican,[7] Luigi Mancini,[2] John Southworth,[8] Adam Greenberg,[7] Jake D. Turner,[9] Robert Thompson,[1] Brian W. Taylor,[10] Stephen E. Levine[11,12] and Matthew W. Webber[12]

Affiliations are listed at the end of the paper

Accepted 2014 June 17. Received 2014 June 11; in original form 2013 October 29

ABSTRACT

It is important to explore the diversity of characteristics of low-mass, low-density planets to understand the nature and evolution of this class of planets. We present a homogeneous analysis of 12 new and 9 previously published broad-band photometric observations of the Uranus-sized extrasolar planet GJ 3470b, which belongs to the growing sample of sub-Jovian bodies orbiting M dwarfs. The consistency of our analysis explains some of the discrepancies between previously published results and provides updated constraints on the planetary parameters. Our data are also consistent with previous transit observations of this system. The physical properties of the transiting system can only be constrained as well as the host star is characterized, so we provide new spectroscopic measurements of GJ 3470 from 0.33 to 2.42 μm to aid our analysis. We find $R_* = 0.48 \pm 0.04$ R$_\odot$, $M_* = 0.51 \pm 0.06$ M$_\odot$, and $T_{\rm eff}$ = 3652 ± 50K for GJ 3470, along with a rotation period of 20.70 ± 0.15 d and an *R*-band amplitude of 0.01 mag, which is small enough that current transit measurements should not be strongly affected by stellar variability. However, to report definitively whether stellar activity has a significant effect on the light curves, this requires future multiwavelength, multi-epoch studies of GJ 3470. We also present the most precise orbital ephemeris for this system: $T_o = 2455983.70472 \pm 0.00021BJD_{\rm TDB}$, $P = 3.336\,6487^{+0.000\,0043}_{-0.000\,0033}$ d, and we see no evidence for transit timing variations greater than 1 min. Our reported planet to star radius ratio is 0.076 42 ± 0.000 37. The physical parameters of this planet are $R_{\rm p} = 3.88 \pm 0.32$ R$_\oplus$ and $M_{\rm p} = 13.73 \pm 1.61$ M$_\oplus$. Because of our revised stellar parameters, the planetary radius we present is smaller than previously reported values. We also perform a second analysis of the transmission spectrum of the entire ensemble of transit observations to date, supporting the existence of an H_2-dominated atmosphere exhibiting a strong Rayleigh scattering slope.

Key words: techniques: photometric – techniques: spectroscopic – eclipses – planets and satellites: atmospheres – stars: individual: GJ 3470– infrared stars.

1 INTRODUCTION

It is important to pursue detailed characterization of extrasolar planets between Earth and Neptune-mass because these bodies have no Solar system analogue, and may provide key insight into the mechanisms of formation and evolution of planetary systems. The *Kepler* mission has discovered over 2300 planet candidates as of 2012 February (Batalha et al. 2013), analysis of which yields increasing occurrence with decreasing planet radius (Howard et al. 2012; Dressing & Charbonneau 2013; Dong & Zhu 2013). Despite the relative abundance of sub-Jovian exoplanets, few have been characterized in great detail. The majority of the *Kepler* candidates pose a challenge when detecting transits from the ground because they do

⋆ E-mail: lbiddle@email.arizona.edu

not meet the criteria for sufficient precision capabilities (e.g. they lack either a large planet-to-star radius ratio or a bright host star). However, these requirements are fulfilled for planets that transit nearby M dwarfs. These systems allow significantly smaller extrasolar planets to be studied with greater precision because they exhibit larger transit depths (Deming, Richardson & Harrington 2007; Demory et al. 2007; Gillon et al. 2007) than if they were to orbit a larger, dimmer star. Per contra, such observationally favourable systems that exhibit a deep transit are relatively rare. So far, the only other small, low-mass planets that can be thoroughly characterized are GJ 436b (Butler et al. 2004; Gillon et al. 2007), GJ 1214b (Charbonneau et al. 2009), and HD 97658b (Howard et al. 2011; Dragomir et al. 2013) with the exception of 55 Cnc e, which orbits a solar-type star (McArthur et al. 2004; Dawson & Fabrycky 2010; Demory et al. 2011; Winn et al. 2011). It is essential to probe this population to compare these systems' properties with those of the more thoroughly studied hot Jupiters so that we may develop our understanding of formation mechanisms of planets linking Earth and Jupiter analogues.

A recent addition to this collection of exoplanets is GJ 3470b (Bonfils et al. 2012), a warm ice giant roughly the size and mass of Uranus orbiting a nearby M dwarf. This system exhibits a sufficiently large transit depth to make detailed characterization of the planet feasible. Previous studies of GJ 3470b probe the planet's atmospheric composition: Fukui et al. (2013) present optical transit photometry and tentatively claim that the planet does not have a thick cloud layer. Crossfield et al. (2013) presented *K*-band transit spectroscopy and found a flat transmission spectrum consistent with a hazy, methane-poor, or high-metallicity atmosphere. Optical photometry indicates a strong Rayleigh-scattering slope at short wavelengths also consistent with a hazy atmosphere (Nascimbeni et al. 2013).

Several effects can interfere with measurements, posing limitations on our understanding of GJ 3470b's bulk properties and atmospheric constraints. For example, when occulted by the planet, star-spots introduce wavelength-dependent perturbations into the light curve and the resulting transit parameters (e.g. Pont et al. 2007; Rabus et al. 2009). Unocculted star-spots can have an effect on the transit depth, making it appear larger than it would without stellar activity (Guillot & Havel 2011; Jordán et al. 2013). Furthermore, the amount of star-spots visible on the Earth-directed face of the star varies over time because of stellar rotation and star-spot evolution, and will be different for observations taken over several epochs, e.g. Czesla et al. (2009), Knutson et al. (2011), and Pont et al. (2013). To account for these factors, we utilize long-term photometric monitoring to assist in identifying these time-dependent changes in stellar brightness, and our results predict a weak systematic effect on the data due to stellar activity.

Our photometric campaign of GJ 3470b, consisting of 12 new transit observations in conjunction with nine previously published light curves, aims to enhance measurements of planetary radius and mass, in addition to placing further constraints on the planetary atmosphere. The analysis also provides an improved ephemeris, which can assist in the eventual search for additional planetary bodies in the GJ 3470 system via observed variations in transit timing (Agol et al. 2005; Holman & Murray 2005). A repercussion of photometric follow-up of planetary systems is the opportunity to provide more accurate estimates of stellar properties. Improved constraints on GJ 3470 increase the precision with which we can derive planetary parameters. Thus, we also present revised stellar parameters that improve upon those previously derived for GJ 3470 (Bonfils et al. 2012; Demory et al. 2012; Fukui et al. 2013; Pineda, Bottom & Johnson 2013) using visible and near-IR spectra.

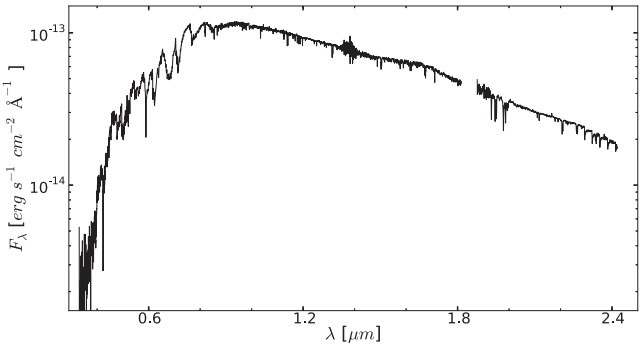

Figure 1. The stellar spectrum of GJ 3470 from 0.33 to 2.42 μm obtained with UH 2.2 m/SNIFS (0.33–0.9 μm) and IRTF/SpeX (0.9−2.4 μm). The noisy regions around 1.4 and 1.9 μm are due to telluric contamination. These data are available as an electronic supplement to the paper.

In this paper, we provide improved planetary, orbital, and stellar parameters for the GJ 3470 system. We also include a revision of stellar properties, and possible sources of systematic error. We begin with host star characterization in Section 2, which includes data acquisition, reduction processes, and results. In Section 3, we describe observations, data calibration, and results for the planetary system. Discussion of the significance of these results takes place within Section 4. We conclude in Section 5.

2 STELLAR SPECTROSCOPY AND LONG-TERM PHOTOMETRIC MONITORING

Having detailed knowledge of an exoplanet's host star is crucial in the understanding of the planetary system. Properties such as planet mass and radius are determined only as precisely as the corresponding stellar properties are known. Bulk and spectral properties help constrain the system age and stellar metallicity, and potentially help determine conditions that influence the formation of planetary systems. The following section describes our observations of GJ 3470, which we use to characterize the stellar parameters in Section 4.1.

The stellar spectra obtained with IRTF/SpeX (Section 2.1.1) and UH/SNIFS (Section 2.1.2) are plotted in a single figure (Fig. 1). These data are also available as an electronic supplement.

2.1 Spectroscopic observations and data reduction

2.1.1 IRTF (3 m)/SpeX

We observed GJ 3470 with SpeX (Rayner et al. 1998) at the 3 m NASA IRTF on UT 2013-02-28, and obtained spectra from 0.9 to 2.4 μm using a 0.3 arcsec slit, which provides spectral resolution of roughly 2000. We obtained 20 frames, each of 20 s duration. Observations were obtained with the slit aligned at the parallactic angle. Data reduction followed previously described methods (Rayner, Cushing & Vacca 2009; Crossfield 2012); in brief, we used the XSPEXTOOL package (Cushing, Vacca & Rayner 2004) to calibrate raw frames, extract spectra from nod-subtracted frames, correct for telluric absorption using observations of the A0V star HD 58296 (obtained at slightly higher airmass: 1.17 versus 1.13), and combine multiple echelle orders into a single spectrum. The final signal-to-noise ratio (SNR) of our spectrum ranges from 150 to 370 pix^{-1}. We flux-calibrate the spectrum using previously described methods (Rayner et al. 2009).

2.1.2 UH (2.2 m)/SNIFS

Optical spectra of GJ 3470 were obtained from 0.33 to 0.9 μm with the SuperNova Integral Field Spectrograph (SNIFS; Aldering et al. 2002; Lantz et al. 2004) on the University of Hawaii 2.2 m telescope atop Mauna Kea. SNIFS separates the incoming light into blue (3200–5200 Å) and red (5100–9700 Å) spectrograph channels, yielding resolutions of ≃800 and ≃1000, respectively. An integration time of 85 s was sufficient to achieve a peak SNR of ≃200 pix^{-1} in the red and ≃70 in the blue.

The SNIFS pipeline (Bacon et al. 2001; Aldering et al. 2006) performed basic reduction, including bias, flat-field, and dark corrections. The spectrum was wavelength calibrated using arc lamp exposures taken at the same telescope pointing and time as the science data. Over the course of each night, we obtained spectra of the EG131 and Feige 110 spectrophotometric standards (Oke 1990; Hamuy et al. 1992; Bessell 1999). We combined a model of telluric absorption from Buton et al. (2013) with standard star observations to correct each spectrum for instrument response and atmospheric extinction. We shifted each spectrum in wavelength to the rest frames of their source stars by cross-correlating each spectrum to a spectral template of similar spectral type from the Sloan Digital Sky Survey (Stoughton et al. 2002; Bochanski et al. 2007). More details on our data reduction can be found in Mann et al. (2012) and Lépine et al. (2013).

2.2 Long-term photometric monitoring

We obtained nightly photometry of GJ 3470 with the Tennessee State University Celestron C14 0.36 m Automated Imaging Telescope (AIT) located at Fairborn Observatory in southern Arizona (Henry 1999; Eaton, Henry & Fekel 2003). The AIT is equipped with an SBIG STL-1001E CCD camera and a Cousins *R* filter. Each observation consists of 4–10 consecutive exposures on a field containing GJ 3470 and several surrounding comparison stars. The individual frames are then co-added and reduced to differential magnitudes (i.e. GJ 3470 minus the mean brightness of the comparison stars). Each nightly observation is also corrected for differential extinction. A total of 246 nightly observations (excluding transit observations) were collected between 2012 December 10 and 2013 May 27.

The nightly out-of-transit observations range over 169 d of the 2012–2013 observing season and are plotted in the top panel of Fig. 2. Brightness variability with a period of ∼20 d and an amplitude of ∼0.01 mag is easily seen by inspection of the light curve. A frequency spectrum, based on the least-squares fitting of sine curves to unequally spaced observations, was computed via the method of Vaníček (1971) and plotted in the middle panel of Fig. 2 as the reduction of the variance in the data versus trial period. The best frequency corresponds to a period of 20.70 ± 0.15 d, where the uncertainty is estimated from the width of the highest peak. We take this to be the star's rotation period, made apparent by rotational modulation in the visibility of star-spots. This rotation period agrees well with the low $v\sin(i)$ measured by Bonfils et al. (2012). The observations are replotted in the bottom panel phased with the rotation period and overlaid with a least-squares sine fit to the phased observations. The peak-to-peak amplitude is only 0.010 mag suggesting that an analysis of the transit observations will not have to deal with complications caused by the planetary occultation of large spots. The sine-curve fit in the bottom panel is converted to HJD and overlaid on the observations in the top panel, and shows good coherence in spite of the small spot amplitude. Henry,

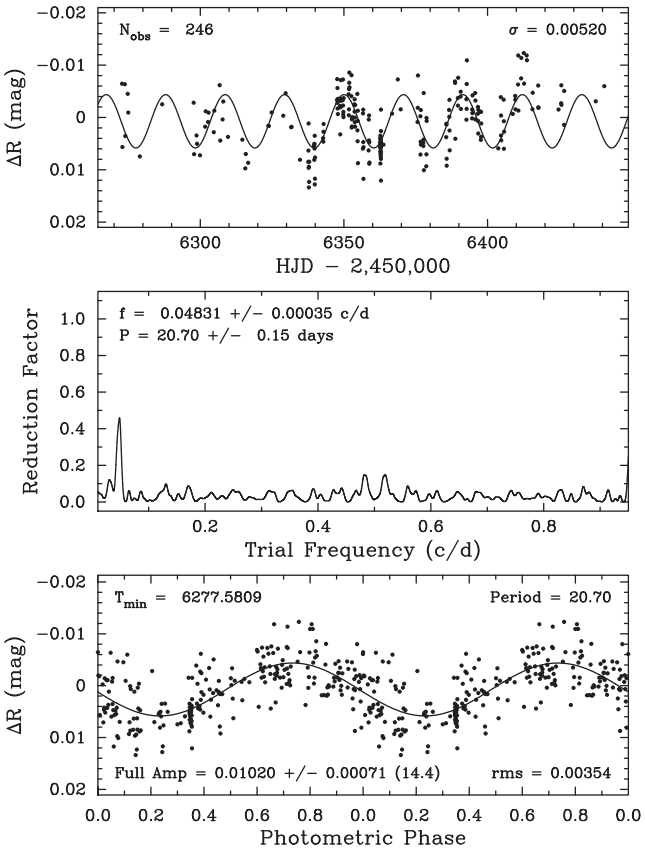

Figure 2. Top: the Cousins *R*-band photometry of GJ 3470 (see Section 2.2) from 2012 to 2013 acquired with the C14 0.36 m AIT at Fairborn Observatory. Slow brightness variability of 0.01 mag or so is apparent. Middle: frequency spectrum of the C14 observations gives a stellar rotation period of 20.70 ± 0.15d. Bottom: a least-squares sine fit of the C14 observations phased with 20.70-d rotation period shows reasonable coherence over the 2012–2013 observing season. This same sine curve is laid over the photometric observations in the top panel and also shows good coherence in spite of the small spot amplitude.

Fekel & Hall (1995) show additional detections of low-level brightness variability in several dozen moderately active stars.

We phased the photometric observations to the radial velocity (RV) period and computed a new least-squares sine fit to the RV period. The formal peak-to-peak amplitude is 0.000 59 ± 0.000 99 mag. This is consistent with the lack of detection of the photometric signal in the radial velocities of Bonfils et al. (2012) and confirms that RV variations in GJ 3470 are indeed due to planetary reflex motion and not line-profile variations due to spots (e.g. Queloz et al. 2001; Paulson et al. 2004). Furthermore, these variations support that there is no consequential systematic effect on the transit light curves (see Section 4.1.3).

3 TRANSIT LIGHT CURVES: DATA AND ANALYSIS

In this section, we describe our observations and calibration methods. We also discuss our light-curve analysis procedure and results.

3.1 Photometric observations and analysis

We obtained 12 total light curves (five full and seven partial), in which many of the events were observed with multiple facilities.

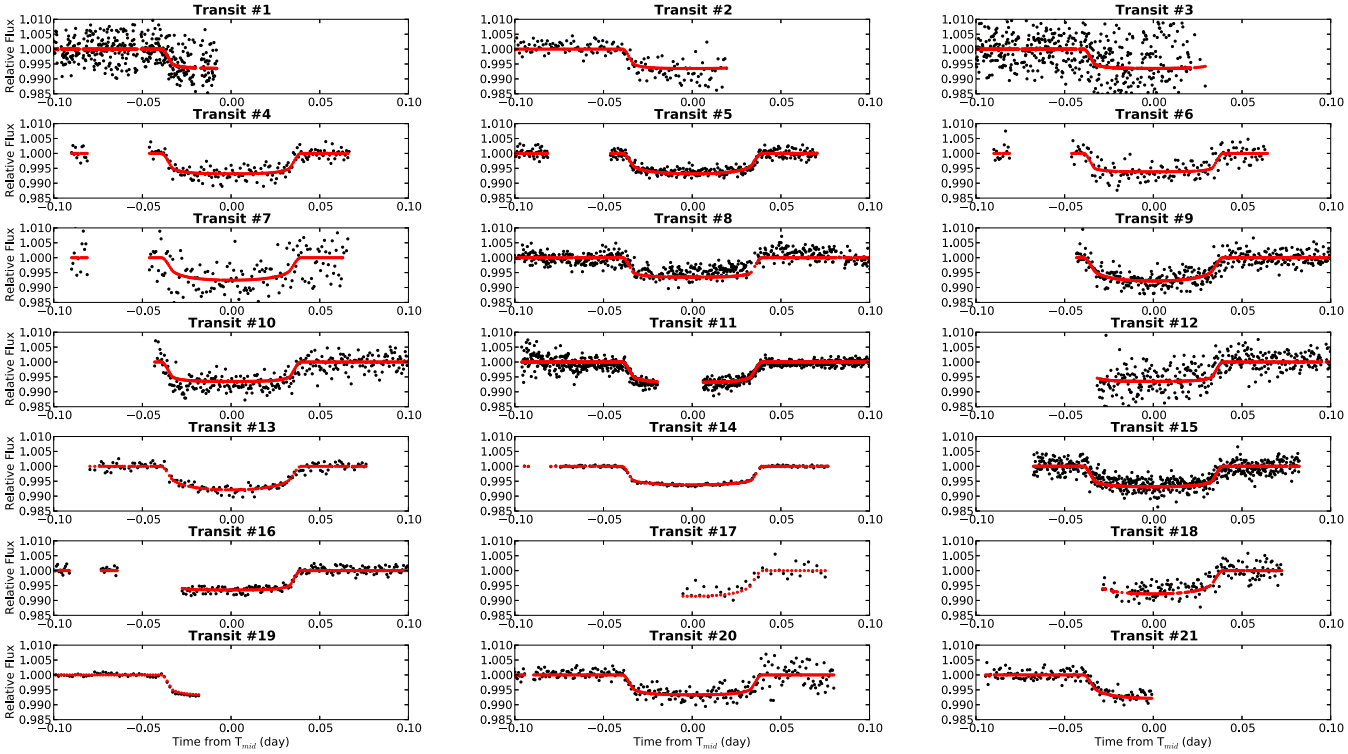

Figure 3. Individual light curves of GJ 3470b are associated with the transit number found in Table 1. The best-fitting model is shown as a solid red line. These data and the residuals are available as an electronic supplement to the paper.

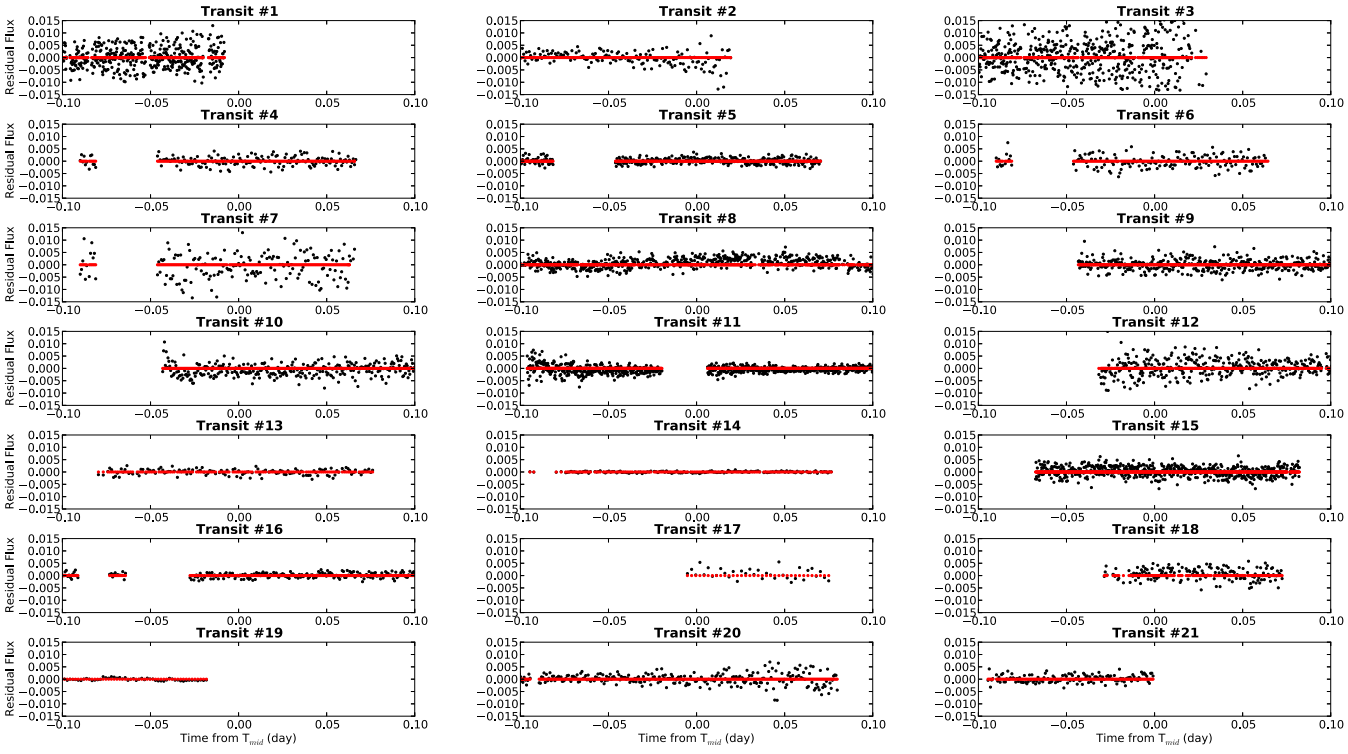

Figure 4. Corresponding residuals for the individual light curves in Fig. 3.

We also include nine light curves previously analysed by Bonfils et al. (2012), Fukui et al. (2013), and Nascimbeni et al. (2013) for a total of 21 light curves analysed homogeneously. All light curves analysed in this work are plotted in Fig. 3, and the corresponding residuals are displayed in Fig. 4. Observational details including integration time, airmass range, and median seeing are summarized in Table 1, and the data acquisition process and reduction methods are described below.

Table 1. Individual transit log and parameters.

Transit	Date (UT)	Filter	Telescope	Exposure time	Airmass	Seeing	R_p/R_*	T_{mid} [$BJD_{TDB} - 245\,0000$]
01[a]	2012 Feb 26	Gunn *Z*	Trappist	10 s	1.4–1.9	–	$0.0766^{+0.0019}_{-0.0020}$	5983.7417±0.0015
02[a]	2012 Mar 07	Gunn *Z*	EulerCam	50 s	>3.55	–	$0.0766^{+0.0019}_{-0.0020}$	5993.7141±0.0015
03[a]	2012 Mar 07	Gunn *Z*	Trappist	10 s	>3.04	–	$0.0766^{+0.0019}_{-0.0020}$	5993.7141±0.0015
04[b]	2012 Nov 15	I_c	MITSuME	60 s	1.06–1.28	Defocused	$0.0780^{+0.0015}_{-0.0016}$	$6247.29954^{+0.00028}_{-0.00029}$
05[b]	2012 Nov 15	*J*	ISLE	30 s	1.06–1.42	Defocused	$0.0757^{+0.0012}_{-0.0013}$	$6247.29954^{+0.00028}_{-0.00029}$
06[b]	2012 Nov 15	R_c	MITSuME	60 s	1.06–1.28	Defocused	$0.0752^{+0.0039}_{-0.0044}$	$6247.29954^{+0.00028}_{-0.00029}$
07[b]	2012 Nov 15	g'	MITSuME	60 s	1.06–1.28	Defocused	$0.0786^{+0.0080}_{-0.011}$	$6247.29954^{+0.00028}_{-0.00029}$
08	2012 Nov 22	Gunn *Z*	Nickel	65 s	1.0–1.2	1.5 arcsec	$0.0766^{+0.0019}_{-0.0020}$	$6253.9729^{+0.0011}_{-0.0013}$
09	2013 Jan 08	r'	LSC	20 s	1.0–1.8	2.7 arcsec	0.0803±0.0025	$6300.68551^{+0.00063}_{-0.00068}$
10	2013 Jan 08	Panstarrs-*Z*	LSC	30 s	1.0–1.8	2.2 arcsec	$0.0766^{+0.0019}_{-0.0020}$	$6300.68551^{+0.00063}_{-0.00068}$
11	2013 Jan 18	*I*	DCT	10 s	1.1–2.0	Defocused	$0.0780^{+0.0015}_{0.0016}$	$6310.69616^{+0.00032}_{-0.00031}$
12	2013 Jan 18	Gunn *Z*	Nickel	65 s	1.3–2.0	1.5 arcsec	$0.0766^{+0.0019}_{-0.0020}$	$6310.69616^{+0.00032}_{-0.00031}$
13[c]	2013 Feb 17	LBC Uspec	LBT	60 s	1.0–1.2	dDefocused	0.0792±0.0019	$6340.72589^{+0.00012}_{-0.00013}$
14[c]	2013 Feb 17	LBC F972N20	LBT	60 s	1.0–1.2	Defocused	0.07430±0.00072	$6340.72589^{+0.00012}_{-0.00013}$
15	2013 Feb 17	Arizona-*I*	Kuiper	07 s	1.04–1.27	1.43 arcsec	$0.0736^{+0.0029}_{-0.0031}$	$6340.72589^{+0.00012}_{-0.00013}$
16	2013 Feb 27	Gunn *Z*	Nickel	65 s	1.0–1.2	1.5 arcsec	$0.0766^{+0.0019}_{-0.0020}$	$6350.73524^{+0.00088}_{-0.00090}$
17	2013 Mar 09	Bessel-*B*	FTN	180 s	1.0–1.1	2.7 arcsec	$0.084^{+0.013}_{-0.016}$	$6360.7449^{+0.0012}_{-0.0015}$
18	2013 Mar 09	r'	ELP	30 s	1.0–1.7	Defocused	0.0803±0.0025	$6360.7449^{+0.0012}_{-0.0015}$
19	2013 Mar 15	Cousins *I*	CAHA 1.23-m	120 s	1.11–1.15	Defocused	$0.0780^{+0.0015}_{-0.0016}$	$6367.41949^{+0.00045}_{-0.00043}$
20	2013 Mar 19	i'	ELP	45 s	1.0–2.6	Defocused	$0.0765^{+0.0027}_{-0.0030}$	$6370.75641^{+0.00081}_{-0.00076}$
21	2013 Mar 29	r'	ELP	45 s	1.0–2.9	Defocused	0.0803±0.0025	$6380.76480^{+0.00083}_{-0.00080}$

[a] First presented by Bonfils et al. (2012), reanalyzed here.
[b] First presented by Fukui et al. (2013), reanalyzed here.
[c] First presented by Nascimbeni et al. (2013), reanalyzed here.

3.1.1 *Discovery Channel Telescope (4 m)*

We observed a full transit during early science observations with the Discovery Channel Telescope's Large Monolithic Imager (LMI), an E2V CCD-231, 6 k × 6 k, deep depletion CCD and a field of view (FOV) of 12.3 arcmin × 12.3 arcmin. Data were taken with the LMI's Cousin *I* filter.[1] Ingress occurred as GJ 3470 was rising (airmass 1.8) so the pre-ingress photometry exhibits higher scatter than the subsequent data. Because DCT's audible warning alarms had not yet been activated, a partial dome occultation occurred in the middle of the transit and we excise these data from the subsequent analysis. Observations were made with a significant amount of defocus in order to maximize integration times and reduce overheads. To avoid possible systematic drifts from the LMI's four-quadrant readout, we measure photometry only for GJ 3470 and two comparison stars lying within a single quadrant of the detector. We investigate a wide range of aperture sizes, and in the final analysis use a 10 arcsec photometric aperture that minimizes the scatter in the resulting light curve. This observation is denoted as transit number 11 as seen in Table 1.

3.1.2 *Kuiper (1.55 m)*

Three transit observations were conducted at the Steward Observatory Kuiper Telescope in Arizona using the Mont4k CCD 4096 × 4096 pixel sensor with an FOV of 9.7 arcmin × 9.7 arcmin using the red, Arizona-*I* optical filter. Two transits were obtained under poor weather conditions, which was the source of significant amount of scatter in both light curves, yielding extremely low-quality data, so we present the one good light curve (number 15), which was acquired on a clear night.

To reduce the data, we used the Exoplanet Data Reduction Pipeline, ExoDRPL, described by Pearson, Turner & Sagan (2014). We performed standard IRAF aperture photometry using eight comparison stars at 110 different aperture radii. After all combinations of comparison stars were tested, we found that a 6.02 arcsec aperture radius and one comparison star of much the same brightness as GJ 3470 provided the lowest scatter in the pre- and post-transit baseline. We produce a synthetic light curve by averaging the light curves from our reference stars, and normalize the final light curve of GJ 3470b by dividing by this synthetic light curve.

3.1.3 *LCOGT (1 m and 2 m)*

We observed three full and three partial transits using telescopes of the Las Cumbres Observatory Global Telescope (LCOGT) network. All LCOGT 1.0 m data were obtained using an SBIG STX-16803 4096 × 4096 CCD with 0.464 inch square pixels (2 × 2 binning), a 15.8 arcmin × 15.8 arcmin FOV, and processed using the pipeline described in Brown et al. (2013). Two full transits taken in r' and PanStarrs-*Z* bands were acquired with two of the 1.0 m telescopes at the LSC node of the network at the Cerro Tololo Inter-American Observatory in Chile. Two partial transits were observed in Sloan r', and a full transit was acquired in the i' band using the 1.0 m telescope at the ELP node of the network at McDonald Observatory in Texas. The i'-band observations were defocused slightly.

[1] See http://www.lowell.edu/techSpecs/LMI/I.eps.

We obtained a partial transit with the 2.0-m Faulkes Telescope North (FTN), a part of the LCOGT's network of robotic telescopes, using a Fairchild CCD486 BI 4 k × 4 k Spectral Imaging camera with an FOV of 10.5 arcmin × 10.5 arcmin (Brown et al. 2013) in the Bessel-*B* filter. We defocused the telescope moderately in order to avoid saturation and we increased the open shutter time relative to the overhead time. The light curves were extracted through aperture photometry using 5.5 arcsec aperture radii, eight comparison stars for the r'-band observation number 18, and seven comparison stars for i' and r', 20 and 21. We also perform differential photometry using the weighted average of two, six, and seven comparison stars for the r', Panstarrs-*Z*, and *B* time series (9, 10, and 17), respectively. The weather during all observation nights was clear with the exception of transit 18.

3.1.4 Lick/Nickel (1 m)

We observed a total of six observations at the Nickel Telescope at Lick Observatory using the CCD-2 Direct Imaging Camera with a 2048 × 2048 pixel CCD and an FOV of 6.3 arcmin × 6.3 arcmin, with the Gunn *Z* filter. We omit three of these observations because they were taken under poor weather conditions and resulted in low-quality light curves. We do present one full light curve (transit 08) and two partial light curves (transits 12 and 16). All observations were defocused, and counts were kept below 35 000 to preserve linearity. We performed standard aperture photometry methods using two comparison stars of similar magnitude to GJ 3470, and a set of custom IDL routines that were also used for the previous analysis of transit light curves obtained at this facility (Johnson et al. 2011). We selected aperture radii for each light curve that minimized scatter.

3.1.5 Calar Alto/Zeiss (1.23 m)

We observed a partial transit using the Zeiss telescope at the German–Spanish Calar Alto Observatory with the Cousins *I* filter using a DLRMKIII camera, equipped with an E2V CCD231-84-NIMO-BI-DD sensor, 4 k × 4 k pixels of 15 μm and an FOV of 21 arcmin × 21 arcmin, which was already successfully employed to investigate several transiting planets (Ciceri et al. 2013; Mancini et al. 2013). We observed the ingress phase of the transit, but the emergence of clouds prevented us from observing the remainder of the event.

We analysed the data using a version of the DAOPHOT reduction pipeline (Stetson 1987; Southworth et al. 2009). Aperture photometry is then performed using the IDL task, Aper, which is part of NASA's ASTROLIB subroutine library, and we account for pointing variations by cross-correlating each image against a reference image. We chose the aperture size and four comparison stars that yielded the lowest scatter in the final differential photometry light curve. The relative weights of the comparison stars were optimized simultaneously by fitting a second-order polynomial to the outside-transit observations to normalize them to unit flux.

3.2 Methods

To fit our light curves, we use the Transit Analysis Package (TAP), an IDL fitting software written by Gazak et al. (2012). TAP uses Markov Chain Monte Carlo (MCMC) techniques to fit light curves by utilizing the analytical model of Mandel & Agol (2002). While performing the analysis, we ran 100 000 MCMC steps. TAP assesses the uncertainties using the wavelet based likelihood function developed by Carter & Winn (2009), where 'red' noise is the time-correlated Gaussian scatter, and 'white' noise is the uncorrelated Gaussian scatter.

For the analysis process, we allowed the scaled semimajor axis, a/R_*, period, P, and inclination, i, to vary freely, but required they be consistent for the entire data set. The mid-transit time, T_o, could float for each transit, under the requirement that all events are related to each other by a linear ephemeris. We linked the planet to star radius ratio, R_P/R_*, for all transits taken with comparable bandpasses to measure transit depths as a function of wavelength. We accounted for limb darkening by using quadratic law limb-darkening coefficients and corresponding uncertainties calculated using the Monte Carlo approach described by Crossfield et al. (2013), who derive these values using $T_{\rm eff} = 3500$ K, surface gravity of 10^5 cm s^{-2}, and solar abundances. The limb-darkening coefficients varied with Gaussian priors using the coefficients and uncertainties described above, and listed in Table 2. Bonfils et al. (2012) report a 1σ upper limit on GJ 3470b's orbital eccentricity, e, of 0.051. Using the Systemic tool (Meschiari et al. 2009), we estimated that the posterior distribution of orbital eccentricity from the RV discovery data is approximately described by a normal distribution (truncated below zero) with mean 0.009 and dispersion 0.088, consistent with a

Table 2. Filter-specific quadratic limb-darkening coefficients.

Filter	Telescope	Best fit[a,d]	PHOENIX[b,d]	Kurucz[c,d]
r'	ELP/LSC	$0.403^{+0.040}_{-0.044}$, $0.390^{+0.036}_{-0.038}$	0.386 ± 0.044, 0.383 ± 0.032	0.391, 0.329
Gunn *Z*	Lick, Trappist, Euler	$0.017^{+0.014}_{-0.012}$, 0.5030 ± 0.0068	0.013 ± 0.016, 0.503 ± 0.008	0.224, 0.424
Panstarrs-*Z*	LSC	$0.029^{+0.025}_{-0.018}$, 0.5030 ± 0.014	0.022 ± 0.017, 0.522 ± 0.007	0.119, 0.487
I	DCT, CAHA	0.070 ± 0.025, $0.517^{+0.010}_{-0.0099}$	0.066 ± 0.019, 0.517 ± 0.007	0.100, 0.484
Arizona-*I*	Kuiper	$0.083^{+0.035}_{-0.032}$, 0.519 ± 0.016	0.075 ± 0.019, 0.518 ± 0.008	0.179, 0.439
i'	ELP	$0.123^{+0.038}_{-0.047}$, 0.488 ± 0.020	0.123 ± 0.021, 0.489 ± 0.010	0.230, 0.422
J	Okayama	$0.023^{+0.018}_{-0.013}$, 0.383 ± 0.012	-0.009 ± 0.014, 0.383 ± 0.006	−0.119, 0.510
g'	Mitsume	0.359 ± 0.063, $0.412^{+0.051}_{-0.054}$	0.359 ± 0.034, 0.410 ± 0.026	0.392, 0.401
R_c	Mitsume	$0.330^{+0.091}_{-0.069}$, 0.369 ± 0.059	0.371 ± 0.039, 0.373 ± 0.030	0.409, 0.302
I_c	Mitsume	$0.084^{+0.038}_{-0.035}$, $0.5130^{+0.016}_{-0.017}$	0.082 ± 0.020, 0.512 ± 0.008	0.203, 0.423

[a] Final LD coefficients from TAP analysis using the PHOENIX priors shown.
[b] Reference Allard et al. 2011.
[c] Reference Kurucz 1979.
[d] The order of the coefficients listed: first = linear, second = quadratic.

Table 3. Adopted system parameters.

Parameter	Value	Units
Stellar parameters		
Effective temperature[b] $T_{\rm eff}$	3652 ± 50	K
Metallicity[b] [Fe/H]	0.17 ± 0.06	–
Mean density[b] ρ_*	$3.39^{+0.30}_{-0.32}$	$\rho_\odot$
Stellar surface gravity $\log_{10}(g)$	4.78 ± 0.12	cgs
Mass M_*	0.51 ± 0.06	$M_\odot$
Radius R_*	0.48 ± 0.04	$R_\odot$
Distance[a]	28.82 ± 2.53	pc
Rotation period	20.70 ± 0.15	d
Age	1-4	Gyr
Planetary parameters[a]		
Scaled semi-major axis a/R_*	$13.94^{+0.44}_{-0.49}$	–
Planet–star radius ratio $R_{\rm p}/R_*$	$0.076\,42 \pm 0.000\,37$	–
Mid transit time T_o	$2455983.70472 \pm 0.00021$	$\rm BJD_{TDB}$
Orbital period P	$3.336\,6487^{+0.000\,0043}_{-0.000\,0033}$	d
Orbital inclination i	$88.88^{+0.62}_{-0.45}$	deg
Semimajor axis a	0.031 ± 0.0028	au
Impact parameter $b = a\cos i/R_*$	0.29 ± 0.14	–
Mean density $\rho_{\rm p}$	1.18 ± 0.33	g $\rm cm^{-3}$
Surface gravity $\log_{10}(g)$	2.83 ± 0.11	cgs
Mass $M_{\rm p}$	13.73 ± 1.61	$M_\oplus$
Radius $R_{\rm p}$	3.88 ± 0.32	$R_\oplus$
Eccentricity e	$0.017^{+0.016}_{-0.012}$	–
Periastron ω	$1.70^{+0.96}_{-1.20}$	deg
$T_{\rm eq}$	506 - 702	K

[a] The uncertainty in these values are dominated by the uncertainty in the stellar parameters in Section 4.2.
[b] The value for stellar density displayed in this table is the weighted mean of the densities yielded by both the light curves and the spectra in this work. $T_{\rm eff}$ and [Fe/H] provided above are the weighted averages of all previous works, found in Table 4.

circular orbit. We used these values to impose a Gaussian prior on e for the light-curve analysis in TAP.

3.3 Results

The results of the analysis, including $R_{\rm p}/R_*$ and T_o for each light curve, are listed in Table 1. The updated system parameter, a/R_* equals $13.94^{+0.44}_{-0.49}$. We found $P = 3.336\,6487^{+0.000\,0043}_{-0.000\,0033}$ d, and $i = 88.88^{+0.62}_{-0.45}$ deg. Under the assumption there is no wavelength dependence, we take the weighted mean of our wavelength-dependent transit depth measurements, and we find $R_{\rm p}/R_*$ equals $0.076\,42 \pm 0.000\,37$. These values are tabulated in Table 3. The uncertainty on our measurement of $R_{\rm p}/R_*$ is larger than that expected to result from stellar variability (see Section 4.1.3), so GJ 3470's intrinsic variability is unlikely to significantly affect these results.

Using our mid-transit times along with the mid-transit times from Demory et al. (2013), Crossfield et al. (2013), we fit a new linear transit ephemeris, ($T_o = 2455983.70472 \pm 0.00021\rm BJD_{TDB}$, $P = 3.336\,6487^{+0.000\,0043}_{-0.000\,0033}$d). We plot the epoch of each transit against the observed time minus the calculated time (O−C) in Fig. 5. If there were another body orbiting GJ 3470, we might observe a transit timing variation (TTV) due to its gravitational effects on GJ 3470b. Any detectable TTVs must lie outside the timing range labelled in green in Fig. 5, which signifies the upper and lower limits of non-transit variations within 1σ of the error of the period. Any values lying outside of this region indicate deviations from the linear ephemeris as a result of another body in the system. The data point corresponding to Transit 1 does lie outside the region described above; however, this transit coincides with a low-quality, partial light curve, so we disregard this point as a TTV. We find no apparent TTVs in the available data, and within the precision of our measurements.

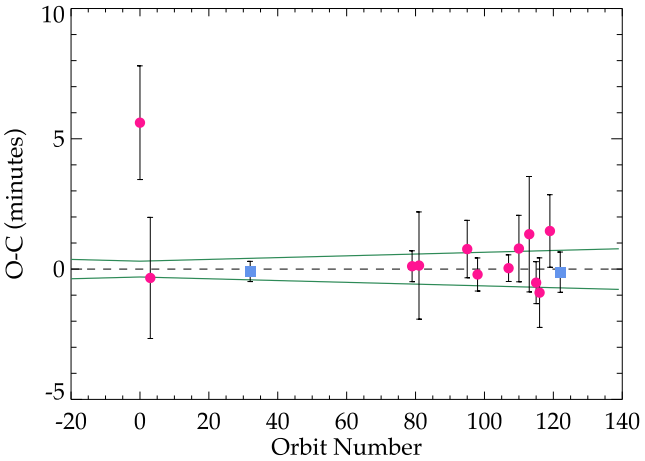

Figure 5. A plot of the observed minus the calculated mid-transit times, where the magenta circles indicate data modelled in this work with TAP, while the blue squares were modelled separately by Demory et al. (2013) and Crossfield et al. (2013). Multiple transits taken at a given epoch share a similar data point. The region outlined in green gives the range of non-TTVs (within 1σ of the error of the period) for each orbit number, beginning with the discovery transit. Values lying outside of this region indicate the occurrence of a TTV. Transit 1 exhibits a low quality, partial light curve; even though it lies outside the region in green, we disregard this point as a TTV.

4 DISCUSSION

The following section discusses implications of the results of stellar characterization, physical system parameters and atmospheric characterization using optical to near-IR transit spectroscopy.

4.1 Stellar characterization

4.1.1 Physical parameters

We determine the metallicity of GJ 3470 using the prescription from Mann et al. (2013a), who provide empirical relations between M dwarf metallicity, [Fe/H], and the strength of molecular and atomic features in visible, *J*, *H*, and *K* bands. We adopt the error-weighted mean of metallicities from each of these relations, accounting for both random and systematic errors. This yields an [Fe/H] of $+0.18 \pm 0.08$.

We deduce the effective temperature, radius, and mass of GJ 3470 by following the procedures in Mann, Gaidos & Ansdell (2013b). To summarize, we compared the optical spectrum to the BT-SETTL version of the PHOENIX atmospheric models (Allard et al. 2013) after masking out a few poorly modelled regions (e.g. TiO at 6500Å). This technique has been shown to reproduce temperatures derived from the bolometric flux and angular diameter of nearby stars (Boyajian et al. 2012) to $\simeq$60 K, which we adopt as the error on our effective temperature. We utilize additional empirical relations from Mann et al. (2013a) relating stellar effective temperature, mass, and radius from nearby stars to calculate the other physical characteristics of the star. We find the stellar effective

Table 4. Stellar parameters.

Reference	Radius ($R_\odot$)	Mass ($M_\odot$)	Stellar density ($\rho_\odot$)	Effective temperature (K)	(Fe/H)
Bonfils et al. (2012)	0.503 ± 0.063	0.541 ± 0.067	4.26±0.53	3600 ± 200	–
Demory et al. (2012)	0.568 ± 0.037	0.539 ± 0.047	2.91 ± 0.37	3600 ± 100	0.2±0.10
Fukui et al. (2013)	0.563 ± 0.024	0.594 ± 0.029	3.32 ± 0.27	–	–
Pineda et al. (2013)	0.500 ± 0.050	0.530 ± 0.050	4.25±0.40	–	0.12±0.12
Crossfield et al. (2013)	–	–	3.49±1.13	–	–
Nascimbeni et al. (2013)	–	–	2.74±0.19	–	–
This work (spectroscopic analysis)	0.48 ± 0.04	0.51 ± 0.06	4.62±1.10	3682 ± 60	0.18±0.08
This work (light curves)	–	–	$3.27^{+0.31}_{-0.34}$	–	–

temperature, $T_{\rm eff} = 3682 \pm 60$ K, stellar radius, $R_* = 0.48 \pm 0.04$ $R_\odot$, and stellar mass, $M_* = 0.51 \pm 0.06$ $M_\odot$.

Under the assumption the planet's orbit is circular, we employed the formula by Seager & Mallén-Ornelas (2003) to independently estimate the stellar density, ρ_*, which follows directly from inverting Kepler's third law of motion by substituting in the expression for mean density in place of mass:

$$\rho_* = \frac{3\pi}{GP^2}\left(\frac{a}{R_*}\right)^3 - \rho_{\rm p}\left(\frac{R_{\rm p}}{R_*}\right)^3, \quad (1)$$

where G is the gravitational constant, P is the orbital period and the second term on the right is typically negligible. We find $\rho_* = 3.27^{+0.31}_{-0.34}$ $\rho_\odot$. These values are tabulated in Table 4.

Our results for the radius of GJ 3470 obtained using the stellar spectrum are lower by more than 1σ than the radii found by Fukui et al. (2013, 0.526 ± 0.023 $R_\odot$) and Demory et al. (2012, 0.568 ± 0.037 $R_\odot$). Our values given above for R_* and M_* alone return a mean bulk density of 4.62 ± 1.10 $\rho_\odot$, roughly 3σ greater than the value derived from our light-curve analysis. We bring attention to the discrepancy in our stellar density derived using the photometric data versus the stellar spectrum. This density offset could indicate a systematic bias caused by occulted or unocculted star-spots, which can be tested by repeated observations and by observations at longer wavelengths. The discrepancy could also be caused by an eccentric orbit, which can be tested further with RV measurements or by determining the time of GJ 3470b's secondary eclipse. Our results support that light curves of transiting planets can help place constraints on the properties of their host stars. However, stellar activity is likely not a contributing factor in our observations because, as mentioned in Section 4.1.3, it is unlikely to pose a significant systematic effect for transit observations, which drives home the necessity of advancing our understanding of M dwarf stars.

In Table 3, we present the final value of ρ_*, which is the weighted mean of both values in this work, deduced from the light curves and spectra. Also provided in Table 3 are the resultant values for the weighted mean of all previously published stellar effective temperatures and metallicities displayed in Table 4, which also lists R_*, M_*, ρ_* for all published studies.

4.1.2 Distance to GJ 3470

We calculate a distance of 28.82 ± 2.53 pc, which is consistent with, and more precise than the value calculated by Pineda et al. (2013, $29.2^{+3.7}_{-3.4}$ pc). Our distance is derived from the fundamental relation between bolometric flux and luminosity ($L_{\rm bol} = 4\pi d^2 F_{\rm bol}$). We use our derived stellar parameters, R_* and $T_{\rm eff}$ (listed in Table 3), to calculate the luminosity for GJ 3470 ($L_{\rm bol} = 4\pi R_\star^2 \sigma T_{\rm eff}^4$). To calculate $F_{\rm bol}$, we integrate the spectrum presented in Section 2 and Fig. 1 from 0.33 to 2.42 μm. For the mid-infrared, we use the *WISE* photometric measurements of GJ 3470, converting the *WISE* infrared magnitudes into units of flux density using the flux zero-points and effective wavelengths given in Wright et al. (2010). We sum the flux between the *WISE* data points using a linear relation between each pair of adjacent points and add it to our previous flux value. We propagated the errors associated with each photometric point using the formula obtained by taking a Taylor expansion for the trapezoidal rule.

To account for the missing flux between the two data sets, we scaled a PHOENIX BT-SETTL model (Allard, Homeier & Freytag 2011) to our measured spectrum and added the integrated model flux between 2.42 and 3.35 μm to the pre-existing bolometric flux obtained using the two spectra. The model used was interpolated from the four nearest spectra in the BT-SETTL compilation to resemble GJ 3470 using the specified parameters $T_{\rm eff} = 3652 \pm 50$K, $\log_{10}(g) = 4.78 \pm 0.12$ and [Fe/H] = 0. To determine the resulting error associated with incorporating the model flux, we scaled the pre-existing error to the percentage of the total additional flux compared to the initial, observed flux (1.063).

Furthermore, to account for the fractional flux shortwards of 0.3 μm and longwards of 22 μm, we scaled our bolometric flux by 1.0362 (determined by the fraction of flux in those regions compared to total stellar flux using the BT-SETTL model). We refrain from altering our uncertainty because the fraction of flux in those regions was much smaller than our other uncertainties and is negligible. We find an apparent bolometric flux of 1.42×10^{-9} [erg cm^{-2} s^{-1}]. The uncertainty on $F_{\rm bol}$ is a few per cent, based on systematic uncertainties in calibrating ground-based spectra (Rayner et al. 2009).

To confirm our calculations, we determined an appropriate geometric scale factor by integrating our measured spectrum, BT-SETTL model, and *WISE* data (where applicable) over three different contiguous bandpasses (0.6–0.8 μm, 2.1–2.3 μm, and 3.3–4.6 μm) and found the mean ratio between the two quantities. The geometric scale factor is proportional to $(R_*/{\rm dist})^2$ and using our previously derived value for R_*, we found that the distance is consistent with our previously derived value. Additionally, we find the values above also yield a distance consistent with that derived using optical bolometric corrections in Flower (1996).

4.1.3 Stellar variability, rotation, and age

GJ 3470's 20 d rotation period (described in Section 2.2) permits an independent estimate of the star's age, previously estimated to be 0.3–3 Gyr (Bonfils et al. 2012). Analysis of Kepler photometry of M dwarf rotation periods shows two distinct groups of stars, with an inferred age ratio between the groups of ∼2.5–3 (McQuillan, Aigrain & Mazeh 2013). GJ 3470's rotation period places it in the more rapidly rotating group; assuming that the slower rotators have ages of 5–10 Gyr then GJ 3470 has an age of roughly 2–4 Gyr. This

gyrochronological age is also broadly consistent with the MEarth survey's analysis of M stars' rotation periods (Irwin et al. 2011). Alternatively, we note also that GJ 3470's rotation period is roughly 1.5 times longer than observed for stars with comparable $V - K$ colours in the 0.6 Gyr Hyades and Praesepe clusters (Delorme et al. 2011). Assuming a rotational braking index of 0.5–0.6, the relations of Meibom, Mathieu & Stassun (2009) imply an age of roughly 1.3 Gyr. We therefore estimate GJ 3470's age to be 1–4 Gyr, consistent with but slightly older than previous estimates (Bonfils et al. 2012).

Using the formalism of (Berta et al. 2011), our measurement of ∼1 per cent peak-to-valley variability in GJ 3470 implies a time-dependent, spot-induced variability in the *R*-band transit depths of 5×10^{-5} over the star's rotation period. Assuming that the spots are 300 K cooler than the stellar photosphere, this effect is roughly 20 per cent larger in *B* band and roughly three times smaller at Warm *Spitzer* wavelengths. This amplitude is smaller than the transit precision from our ensemble of light curves. The precision of the 4.5 μm transit measurement from *Spitzer* (Demory et al. 2013) is also larger than our estimate. Future multiwavelength, multi-epoch studies of GJ 3470b's transits will determine whether stellar activity poses a significant systematic effect for transit observations of this system.

4.2 Physical properties of the planetary system

The values derived from our data analysis (see Table 3) were used to calculate the planetary parameters of GJ 3470b, including its mass, radius, density, equilibrium temperature, surface gravity, and semimajor axis.

We adopted the formula by Southworth, Wheatley & Sams (2007) to calculate the surface gravitational acceleration, $g_{\rm p}$:

$$g_{\rm p} = \frac{2\pi}{P}\left(\frac{a}{R_{\rm p}}\right)^2 \frac{\sqrt{1-e^2}}{\sin i} K_*, \quad (2)$$

where K_* is the stellar velocity amplitude equal to 9.2 ± 0.8 m s^{-1} (Bonfils et al. 2012) and assuming $e = 0$ (justified by current data; see Section 3.2).

The equilibrium temperature, $T_{\rm eq}$, was derived using the relation (Southworth 2010):

$$T_{\rm eq} = T_{\rm eff}\left(\frac{1-A}{4F}\right)^{1/4}\left(\frac{R_\star}{2a}\right)^{1/2}, \quad (3)$$

where $T_{\rm eff}$ is the effective temperature of the host star at 3652 ± 50 K (see Table 4), A is the Bond albedo, and F is the heat redistribution factor. Assuming $A = 0{-}0.4$ and $F = 0.25{-}0.50$, we find the range $T_{\rm eq} = 506$–702 K.

We calculated the planetary mass, $M_{\rm p}$, using the following equation (Winn 2010; Seager 2011):

$$M_{\rm p} = (11.18)\left(\frac{K_\star}{\sin i}\right)\left(\frac{P}{1{\rm yr}}\right)^{1/3}\left(\frac{M_\star}{{\rm M}_\odot}\right)^{2/3} {\rm M}_\oplus, \quad (4)$$

where K_* is the RV semi-amplitude equal to 9.2 ± 0.8 m s^{-1} (Bonfils et al. 2012). For M_* and P, we use the values derived from our analysis (see Table 4). The resultant planetary mass is $M_{\rm p} = 13.73 \pm 1.61$ M$_\oplus$.

Results of the $M_{\rm p}$, $R_{\rm p}$, $\log_{10}(g_{\rm p})$, and the planetary density ($\rho_{\rm p}$) from our analysis are summarized in Table 3. We find a planetary radius of $R_{\rm p} = 3.88 \pm 0.32$ R$_\oplus$.

4.3 Atmospheric constraints

The result of this work compared with previous optical and near-IR studies (Bonfils et al. 2012; Crossfield et al. 2013; Fukui et al. 2013) indicates GJ 3470b appears to have a planetary radius independent of wavelength in the optical through near-IR wavelengths accessible from the ground. However, the recent publication by Nascimbeni et al. (2013) indicates GJ 3470b's radius increases in the direction of the blue side of the spectrum, exhibiting a colour dependence. The recent estimate on the low mean molecular weight of GJ 3470b (Nascimbeni et al. 2013) favours an atmosphere dominated by clouds or haze. It is interesting to note that the atmospheric models presented by Nascimbeni et al. (2013) do not predict the *K*-band measurements of Crossfield et al. (2013), just as the Crossfield et al. (2013) models do not predict the *U*-band measurement of Nascimbeni et al. (2013).

We compare the full ensemble of transit observations of GJ 3470b to a set of model atmospheric transmission spectra. For this purpose, we used the atmospheric models of GJ 3470b presented in Crossfield et al. (2013), which provide model observed transmission spectra after computing self-consistent equilibrium atmospheric chemistry and thermal structure. We allow each model to be scaled by a constant multiplicative factor to account for differences of a few per cent between the observed and modelled transit depths. In light of the recent detection of Rayleigh scattering (Nascimbeni et al. 2013), we include a second analysis in which an ad hoc Rayleigh-scattering haze is added to each transmission spectrum by allowing the slope and offset of the Rayleigh-scattering signature to vary in each fit. We parametrize the haze signature as $R_{\rm P}^{\rm haze} = A - B \ln \frac{\lambda}{1\,\mu{\rm m}}$ (Lecavelier Des Etangs et al. 2008), and take as our final transmission model the greater value of $R_{\rm P}^{\rm haze}$ or the original model at each wavelength. Thus, our haze model is not physically self-consistent, but it captures the essential features observed. For each hazy or haze-free model, we computed χ^2 and the Bayesian Information Criterion (BIC $= \chi^2 + k \ln n$ when fitting n measurements with a k-dimensional model; Schwarz 1978), which penalizes models that use too many parameters. Thus, $k = 3$ for the hazy models and unity for the haze-free models.

The results of this analysis are compiled in Table 5, and we show the three best-fitting models in Fig. 6. The best models all include a Rayleigh-scattering haze, consistent with the results of Nascimbeni et al. (2013). Although the hazy models with supersolar metallicities give a lower χ^2 and BIC than the hazy solar-abundance model, the

Table 5. Atmospheric model fits.

Model name	χ^2	BIC
Hazy, 50 × solar	**8.80**	**17.30**
Hazy, 200 × solar	15.27	23.77
Hazy, Solar	19.15	27.65
200 × solar	29.31	32.14
Flat	32.73	35.56
Hazy, Solar, no CH_4	27.49	35.99
Hazy, Solar, no C	28.66	37.16
Solar, no CH_4	38.83	41.66
Solar, no C	39.59	42.43
Hazy, 200 × , no C	33.94	42.44
50 × solar	39.90	42.73
Hazy, 50 × , no C	39.97	48.47
200 × , no C	45.83	48.67
50 × , no C	57.02	59.86
Solar	62.79	65.62

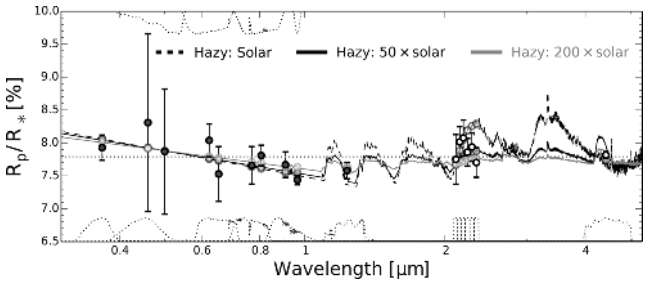

Figure 6. Transmission spectrum of GJ 3470b. Solid points with error bars are our measurements; open points with error bars are previous infrared measurements (Crossfield et al. 2013; Demory et al. 2013). The solid lines show the three best-fitting model transmission spectra described in Section 4.3 and Table 5. These models all include a Rayleigh-scattering slope at shorter wavelengths; no molecular features are yet detected at longer wavelengths. The dotted lines at bottom and top show all filter profiles used in this analysis; we use these to compute the band-integrated model points (shown as coloured open circles).

difference is too small to conclusively determine whether GJ 3470b has a metal-rich atmosphere as do Uranus and Neptune (Lunine 1993) and as proposed for hot Neptune GJ 436b (Fortney et al. 2013; Moses et al. 2013).

5 CONCLUSION

The collection of transits in this work, with the inclusion of the discovery and previously published data, provides improved parameters for the GJ 3470 system and a consistency in the analysis process. In this study, we derived a new set of planetary parameters $M_p = 13.73 \pm 1.61\,M_\oplus$, $R_p = 3.88 \pm 0.32\,R_\oplus$, and $\rho_p = 1.18 \pm 0.33$ g cm^{-3}, all of which are listed in Table 3. We also present, to date, the most precise new transit ephemeris for this system and find an updated period of $3.336\,6487^{+0.000\,0043}_{-0.000\,0033}$ d. Our analysis of possible TTVs indicates little deviation from our calculated ephemeris, but future observations are encouraged to confirm whether or not there are other planetary bodies orbiting GJ 3470.

One benefit of a spectroscopic analysis is the opportunity to provide improved constraints on the host star's properties. The planetary parameters are known only to the accuracy with which we know the star, so it is extremely important to know these values as well. The distance determined agrees with the value found in Pineda et al. (2013). The stellar mass, radius, density, and metallicity (see Table 3) have been updated using a weighted average of our derived stellar parameters and those found in Demory et al. (2012) and Fukui et al. (2013). Different methods of stellar analysis yield varying parameters appropriate for an M dwarf like GJ 3470, which motivates the need for further investigation of M dwarf stars.

This small planet lies in an observationally favourable system that presents the possibility of measuring a transmission spectrum also considered in detail by Fukui et al. (2013), Crossfield et al. (2013), and Nascimbeni et al. (2013).[2] Our second analysis of the entire collection of transit observation agrees with the results of Nascimbeni et al. (2013), suggesting an H_2-dominated Rayleigh-scattering haze. Further observations with higher precision and/or at shorter wavelengths will be necessary to confirm the steep Rayleigh-scattering slope supported in this work and also by Nascimbeni et al. (2013), and to search for molecular absorption features in the planet's transmission spectrum.

[2] Our conclusions are consistent with those of Ehrenreich et al. (2014), which we became aware of seven months after the submission of our work.

ACKNOWLEDGEMENTS

We sincerely thank all of the respective TAC committees responsible for allocating time on the facilities used in our study, as well as the telescope day crews. Special thanks to Dr Elizabeth Green for exchanging observing nights at the Kuiper 1.6 m Telescope to acquire a transit and Rob Zellem for insightful discussion. These results made use of Lowell Observatory's Discovery Channel Telescope, supported by Lowell, Discovery Communications, Boston University, the University of Maryland, and the University of Toledo. The LMI was funded by the National Science Foundation through grant AST-1005313. We also gratefully acknowledge the support from the University of Arizona Astronomy Club. The following internet-based resources were used in this paper: the SIMBAD data base operated by CDS, the ArXiv scientific paper preprint service operated by Cornell University and the ADS operated by the Harvard–Smithsonian Center for Astrophysics.

REFERENCES

Agol E., Steffen J., Sari R., Clarkson W., 2005, MNRAS, 359, 567
Aldering G. et al., 2002, in Tyson J. A., Wolff S., eds, Proc. SPIE, 4836, 61
Aldering G. et al., 2006, ApJ, 650, 510
Allard F., Homeier D., Freytag B., 2011, in Johns-Krull C., Browning M. K., West A. A., eds, ASP Conf. Ser., Vol. 448, 16th Cambridge Workshop on Cool Stars, Stellar Systems, and the Sun. Astron. Soc. Pac., San Francisco, p. 91
Allard F., Homeier D., Freytag B., Schaffenberger W., Rajpurohit A. S., 2013, Mem. Soc. Astron. Ital. Suppl., 24, 128
Bacon R. et al., 2001, MNRAS, 326, 23
Batalha N. M. et al., 2013, ApJS, 204, 24
Berta Z. K., Charbonneau D., Bean J., Irwin J., Burke C. J., Désert J.-M., Nutzman P., Falco E. E., 2011, ApJ, 736, 12
Bessell M. S., 1999, PASP, 111, 1426
Bochanski J. J., West A. A., Hawley S. L., Covey K. R., 2007, AJ, 133, 531
Bonfils X. et al., 2012, A&A, 546, A27
Boyajian T. S. et al., 2012, ApJ, 757, 112
Brown T. M. et al., 2013, PASP, 125, 1031
Butler R. P., Vogt S. S., Marcy G. W., Fischer D. A., Wright J. T., Henry G. W., Laughlin G., Lissauer J. J., 2004, ApJ, 617, 580
Buton C. et al., 2013, A&A, 549, A8
Carter J. A., Winn J. N., 2009, ApJ, 704, 51
Charbonneau D. et al., 2009, Nature, 462, 891
Ciceri S. et al., 2013, A&A, 557, A30
Crossfield I. J. M., 2012, A&A, 545, A97
Crossfield I. J. M., Barman T., Hansen B. M. S., Howard A. W., 2013, A&A, 559, A33
Cushing M. C., Vacca W. D., Rayner J. T., 2004, PASP, 116, 362
Czesla S., Huber K. F., Wolter U., Schröter S., Schmitt J. H. M. M., 2009, A&A, 505, 1277
Dawson R. I., Fabrycky D. C., 2010, ApJ, 722, 937
Delorme P. et al., 2011, MNRAS, 413, 2218
Deming D., Richardson L. J., Harrington J., 2007, MNRAS, 378, 148
Demory B.-O. et al., 2007, A&A, 475, 1125
Demory B.-O. et al., 2011, A&A, 533, A114
Demory B.-O. et al., 2012, Spitzer Proposal, 80261
Demory B.-O. et al., 2013, ApJ, 768, 154
Dong S., Zhu Z., 2013, ApJ, 778, 53

Dragomir D., Matthews J. M., Winn J. N., Rowe J. F. MOST Science Team. 2013, in Haghighipour N., Zhou J.-L., eds, Proc. IAU Symp. 293, Formation, Detection, and Characterization of Extrasolar Habitable Planets. Cambridge Univ. Press, Cambridge, p. 52
Dressing C. D., Charbonneau D., 2013, ApJ, 767, 95
Eaton J. A., Henry G. W., Fekel F. C., 2003, in Oswalt T. D., ed., Astrophysics and Space Science Library, Vol. 288, The Future of Small Telescopes in the New Millennium: Volume II - The Telescope We Use. Kluwer, Dordrecht, p. 189
Ehrenreich D. et al., 2014, A&A, preprint (arXiv:1405.1056)
Flower P. J., 1996, ApJ, 469, 355
Fortney J. J., Mordasini C., Nettelmann N., Kempton E. M.-R., Greene T. P., Zahnle K., 2013, ApJ, 775, 80
Fukui A. et al., 2013, ApJ, 770, 95
Gazak J. Z., Johnson J. A., Tonry J., Dragomir D., Eastman J., Mann A. W., Agol E., 2012, Adv. Astron., 2012, Adv. Astron., 2012, 697967
Gillon M. et al., 2007, A&A, 472, L13
Guillot T., Havel M., 2011, A&A, 527, A20
Hamuy M., Walker A. R., Suntzeff N. B., Gigoux P., Heathcote S. R., Phillips M. M., 1992, PASP, 104, 533
Henry G. W., 1999, PASP, 111, 845
Henry G. W., Fekel F. C., Hall D. S., 1995, AJ, 110, 2926
Holman M. J., Murray N. W., 2005, Science, 307, 1288
Howard A. W. et al., 2011, ApJ, 730, 10
Howard A. W. et al., 2012, ApJS, 201, 15
Irwin J., Berta Z. K., Burke C. J., Charbonneau D., Nutzman P., West A. A., Falco E. E., 2011, ApJ, 727, 56
Johnson J. A. et al., 2011, ApJ, 730, 79
Jordán A. et al., 2013, ApJ, 778, 184
Knutson H. A. et al., 2011, ApJ, 735, 27
Kurucz R. L., 1979, ApJS, 40, 1
Lantz B. et al., 2004, in Mazuray L., Rogers P. J., Wartmann R., eds, Proc. SPIE Vol. 5249, Optical Design and Engineering. SPIE, Bellingham, p. 146
Lecavelier Des Etangs A., Pont F., Vidal-Madjar A., Sing D., 2008, A&A, 481, L83
Lépine S., Hilton E. J., Mann A. W., Wilde M., Rojas-Ayala B., Cruz K. L., Gaidos E., 2013, AJ, 145, 102
Lunine J. I., 1993, ARA&A, 31, 217
McArthur B. E. et al., 2004, ApJ, 614, L81
McQuillan A., Aigrain S., Mazeh T., 2013, MNRAS, 432, 1203
Mancini L. et al., 2013, A&A, 551, A11
Mandel K., Agol E., 2002, ApJ, 580, L171
Mann A. W., Gaidos E., Lépine S., Hilton E. J., 2012, ApJ, 753, 90
Mann A. W., Brewer J. M., Gaidos E., Lépine S., Hilton E. J., 2013a, AJ, 145, 52
Mann A. W., Gaidos E., Ansdell M., 2013b, ApJ, 779, 188
Meibom S., Mathieu R. D., Stassun K. G., 2009, ApJ, 695, 679
Meschiari S., Wolf A. S., Rivera E., Laughlin G., Vogt S., Butler P., 2009, PASP, 121, 1016
Moses J. I. et al., 2013, ApJ, 777, 34
Nascimbeni V., Piotto G., Pagano I., Scandariato G., Sani E., Fumana M., 2013, A&A, 559, A32
Oke J. B., 1990, AJ, 99, 1621
Paulson D. B., Saar S. H., Cochran W. D., Henry G. W., 2004, AJ, 127, 1644
Pearson K. A., Turner J. D., Sagan T. A. G., 2014, New Astron., 27, 102
Pineda J. S., Bottom M., Johnson J. A., 2013, ApJ, 767, 28
Pont F. et al., 2007, A&A, 476, 1347
Pont F., Sing D. K., Gibson N. P., Aigrain S., Henry G., Husnoo N., 2013, MNRAS, 432, 2917
Queloz D. et al., 2001, A&A, 379, 279
Rabus M. et al., 2009, A&A, 494, 391
Rayner J. T., Toomey D. W., Onaka P. M., Denault A. J., Stahlberger W. E., Watanabe D. Y., Wang S.-I., 1998, in Fowler A. M., ed., Proc. SPIE Vol. 3354, Infrared Astronomical Instrumentation. SPIE, Bellingham, p. 468
Rayner J. T., Cushing M. C., Vacca W. D., 2009, ApJS, 185, 289
Schwarz G., 1978, Ann. Stat., 6, 461
Seager S., 2011, in Piper S., ed., Exoplanets. Univ. Arizona Press, Tucson, AZ
Seager S., Mallén-Ornelas G., 2003, ApJ, 585, 1038
Southworth J., 2010, MNRAS, 408, 1689
Southworth J., Wheatley P. J., Sams G., 2007, MNRAS, 379, L11
Southworth J. et al., 2009, MNRAS, 396, 1023
Stetson P. B., 1987, PASP, 99, 191
Stoughton C. et al., 2002, AJ, 123, 485
Vaníček P., 1971, Ap&SS, 12, 10
Winn J. N., 2010, preprint (arXiv:1001.2010)
Winn J. N. et al., 2011, ApJ, 737, L18
Wright E. L. et al., 2010, AJ, 140, 1868

SUPPORTING INFORMATION

Additional Supporting Information may be found in the online version of this article:

(http://mnras.oxfordjournals.org/lookup/suppl/doi:10.1093/mnras/stu1199/-/DC1).

Please note: Oxford University Press is not responsible for the content or functionality of any supporting materials supplied by the authors. Any queries (other than missing material) should be directed to the corresponding author for the paper.

[1]*Department of Astronomy, University of Arizona, 933 N. Cherry Street, Tucson, AZ 85721, USA*
[2]*Max-Planck-Institut für Astronomie, Königstuhl 17, D-69117 Heidelberg, Germany*
[3]*Institute for Astronomy, University of Hawaii at Manoa, 2680 Woodlawn Drive, Honolulu, HI 96822, USA*
[4]*Las Cumbres Observatory Global Telescope Network, 6740 Cortona Drive, Suite 102, Santa Barbara, CA 93117, USA*
[5]*Department of Planetary Sciences, Lunar and Planetary Laboratory, University of Arizona, Tucson, AZ 85721, USA*
[6]*Center of Excellence in Information Systems, Tennessee State University, 3500 John A. Merritt Blvd, Box 9501, Nashville, TN 37209, USA*
[7]*Division of Astronomy and Astrophysics, University of California Los Angeles, 430 Portola Plaza, Los Angeles, CA 90095, USA*
[8]*Astrophysics Group, Keele University, Staffordshire ST5 5BG, UK*
[9]*Department of Astronomy, University of Virginia, 1721 University Avenue, Charlottesville, VA 22903, USA*
[10]*Astronomy Department, Boston University, 725 Commonwealth Ave, Boston, MA 02215, USA*
[11]*Lowell Observatory, 1400 West Mars Hill Road, Flagstaff, AZ 86001, USA*
[12]*Department of Earth, Atmospheric and Planetary Sciences, Massachusetts Institute of Technology, 77 Massachusetts Avenue, Cambridge, MA 02139, USA*

This paper has been typeset from a TEX/LATEX file prepared by the author.